Blaazer, Antoni R., Singh, Abhimanyu K., Zara, Lorena, Boronat, Pierre, Bautista, Lady J., Irving, Steve, Majewski, Maciej, Barril, Xavier, Wijtmans, Maikel, Danielson, U. Helena and others (2024) *The Role of Water Networks in Phosphodiesterase Inhibitor Dissociation and Kinetic Selectivity.* ChemMedChem, 19 (22). ISSN 1860-7187.

The Role of Water Networks in Phosphodiesterase Inhibitor Dissociation and Kinetic Selectivity

Antoni R. Blaazer[+],[a, b] Abhimanyu K. Singh[+],[c, h] Lorena Zara[+],[a] Pierre Boronat,[a] Lady J. Bautista,[a] Steve Irving,[d] Maciej Majewski,[e] Xavier Barril,[e, f] Maikel Wijtmans,[a] U. Helena Danielson,[g] Geert Jan Sterk,[a] Rob Leurs,[a] Jacqueline E. van Muijlwijk-Koezen,[b] David G. Brown,[c] and Iwan J. P. de Esch*[a]

In search of new opportunities to develop *Trypanosoma brucei* phosphodiesterase B1 (TbrPDEB1) inhibitors that have selectivity over the off-target human PDE4 (hPDE4), different stages of a fragment-growing campaign were studied using a variety of biochemical, structural, thermodynamic, and kinetic binding assays. Remarkable differences in binding kinetics were identified and this kinetic selectivity was explored with computational methods, including molecular dynamics and interaction fingerprint analyses. These studies indicate that a key hydrogen bond between Gln$^{Q.50}$ and the inhibitors is exposed to a water channel in TbrPDEB1, leading to fast unbinding. This water channel is not present in hPDE4, leading to inhibitors with a longer residence time. The computer-aided drug design protocols were applied to a recently disclosed TbrPDEB1 inhibitor with a different scaffold and our results confirm that shielding this key hydrogen bond through disruption of the water channel represents a viable design strategy to develop more selective inhibitors of TbrPDEB1. Our work shows how computational protocols can be used to understand the contribution of solvent dynamics to inhibitor binding, and our results can be applied in the design of selective inhibitors for homologous PDEs found in related parasites.

[a]   A. R. Blaazer,[+] L. Zara,[+] P. Boronat, L. J. Bautista, M. Wijtmans, G. J. Sterk, R. Leurs, I. J. P. de Esch
      Division of Medicinal Chemistry, Amsterdam Institute of Molecular and Life Sciences (AIMMS), Vrije Universiteit Amsterdam, De Boelelaan 1108, 1081 HZ Amsterdam, The Netherlands
      E-mail: i.de.esch@vu.nl

[b]   A. R. Blaazer,[+] J. E. van Muijlwijk-Koezen
      Division of Innovations in Human Health & Life Sciences (iH2LS), Amsterdam Institute of Molecular and Life Sciences (AIMMS), Vrije Universiteit Amsterdam, De Boelelaan 1108, 1081 HZ Amsterdam, The Netherlands

[c]   A. K. Singh,[+] D. G. Brown
      School of Biosciences, University of Kent, CT2 7NJ Canterbury, UK

[d]   S. Irving
      Charles River, Ingram Building, Parkwood Road, CT2 7NH Canterbury, UK

[e]   M. Majewski, X. Barril
      Institut de Biomedicina de la Universitat de Barcelona (IBUB), University of Barcelona, Av. Joan XXIII 27, 08028 Barcelona, Spain

[f]   X. Barril
      Catalan Institution for Research and Advanced Studies (ICREA), Passeig Lluís Companys 23, 08010 Barcelona, Spain

[g]   U. H. Danielson
      Science for Life Laboratory, Department of Chemistry-BMC, Uppsala University, SE-75123 Uppsala, Sweden

[h]   A. K. Singh[+]
      Current address A.K.S.: Mahatma Gandhi Medical Advanced Research Institute (MGMARI), Sri Balaji Vidyapeeth (Deemed to be University), Puducherry 607 402, India

[+]   *These authors contributed equally to this work.*

      Supporting information for this article is available on the WWW under https://doi.org/10.1002/cmdc.202400417

Introduction

While developing antiparasitic *Trypanosoma brucei* 3′,5′-cyclic nucleotide phosphodiesterase B1 (TbrPDEB1) inhibitors using biochemically-driven structure-activity relationship (SAR) studies,[1] we learned that it is highly challenging to discover inhibitors that are more potent against TbrPDEB1 than against human PDE4, including the highly similar PDE 4B (hPDE4B) and 4D (hPDE4D) isoforms. This selectivity is important as TbrPDEB1 inhibitors have the potential to treat human African trypanosomiasis, while inhibiting hPDE4 enzymes can lead to gastrointestinal side effects, such as nausea and emesis.[4] In general, low target selectivity is a significant contributor to the failure of PDE inhibitors in clinical trials.[5]

Several studies have shown that the combination of structural data, interaction thermodynamics, and binding kinetics for a congeneric compound series can uncover opportunities for the structure-based design of selective inhibitors, for example, in the case of serine protease inhibitors.[6] Determining the association (k_a or k_{on}) and dissociation (k_d or k_{off}) rate constants, and deriving the residence times (τ or t_r) of a particular series allows the application of structure-kinetic relationships (SKR) in subsequent optimization efforts.[7] Furthermore, an extensive survey of kinase inhibitors has recently highlighted the importance of understanding and achieving kinetic selectivity.[8]

Water plays an important role in protein-ligand binding affinity, and, for example, the effects of displacing a binding-site water molecule or reorganizing the solvent network have been the subject of structure-thermodynamic relationship (STR) studies.[9] However, the understanding of binding kinetics and

ChemMedChem

Research Article
doi.org/10.1002/cmdc.202400417

Chemistry Europe
European Chemical
Societies Publishing

residence time is still limited.[10] It has been shown that the stability of the protein-ligand complex is strongly influenced by solvent effects, such as the re-hydration of the ligand and the binding site during complex dissociation.[11] Also, relevant protein-ligand hydrogen bonds shielded from nearby water molecules are expected to be replaced at slower rates than exposed hydrogen bonds, positively contributing to residence time.[12] Shielding intra-protein hydrogen bonds that confer binding site rigidity can also lead to longer residence times.[13] Furthermore, ligand dissociation from a binding site connected to bulk water through a water channel, as opposed to a water-filled cavity, results in distinct dissociation mechanisms and explains ligand selectivity in two highly similar serine proteases.[14]

To better understand the selectivity profiles and binding kinetics of PDE inhibitors, we selected a representative series of compounds (Figure 1) from a fragment-growing campaign and interrogated the molecular determinants of binding. Structural, kinetic and thermodynamic analyses, first for hPDE4D and then for TbrPDEB1, in combination with computational techniques, allow us to explain the kinetic selectivity of this series. We also demonstrate that our insights can be applied in designing more selective PDE inhibitors.

Results and Discussion

The selected inhibitors **1**–**6** (Figure 1, Table S1 and S2) represent the different stages of a fragment-to-lead effort. The design
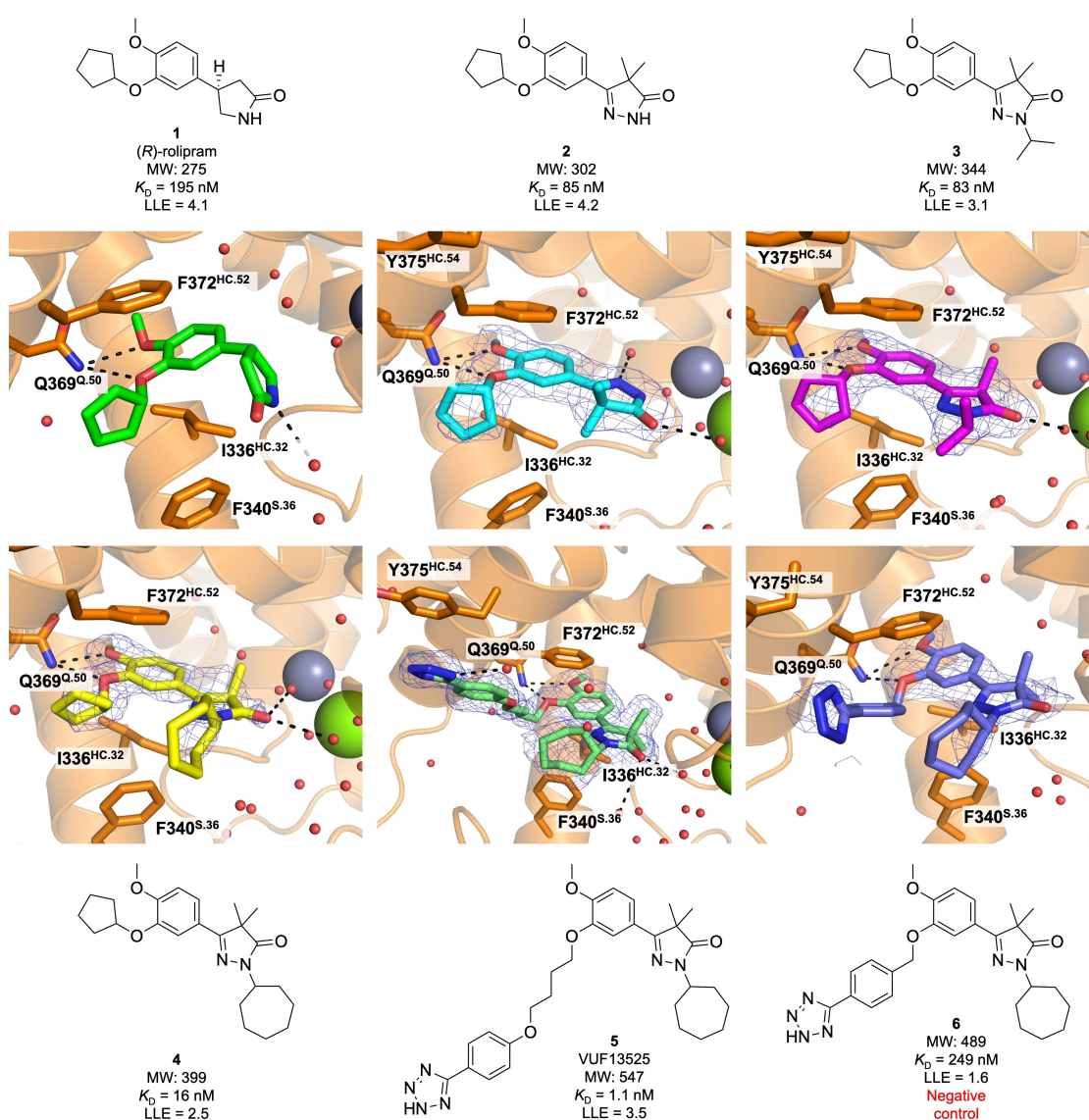
Figure 1. Scaffold hop from rolipram (**1**, PDB code: 1Q9 M) and fragment-to-lead optimization of the pyrazolone-derived PDE inhibitor series **2**–**6**. The hPDE4D co-crystal structures are shown for every compound. Important binding site residues are shown as sticks and labeled according to PDEStrIAn nomenclature,[2] polar interactions are shown as dashed lines in black, water molecules are shown as red spheres, zinc and magnesium cations are displayed as gray and green spheres, respectively, $|F_o - F_c|_{\alpha calc}$ electron density maps contoured at 2.5 σ are shown as a blue mesh, K_D values are derived from the kinetic analysis of SPR biosensor data, ligand-lipophilicity efficiency (LLE) metrics are based on pK_D−cLogP.[3]

ChemMedChem

Research Article
doi.org/10.1002/cmdc.202400417

Chemistry
Europe
European Chemical
Societies Publishing

strategy (Figure S1) involved growing a small fragment-like starting point to reach one of the few differences between the human and parasite PDE proteins: a parasite-specific subpocket known as the P-pocket (Figure S2).[1b] The starting point is the prototypical hPDE4 inhibitor rolipram (1), of which several hPDE4D X-ray co-crystal structures have been reported.[15] This fragment-like (MW < 300) compound binds with its central dialkoxyphenyl moiety to Gln369$^{Q.50}$ and occupies the hydrophobic clamp formed by Ile336$^{HC.32}$ and Phe372$^{HC.52}$ (Figure 1; residue numbers derived from crystal structures, superscript labels according to PDEStrIAn nomenclature as described in Jansen et al.[2]). These fundamental interactions are maintained in all the PDE-inhibitor complexes we obtained. The pyrrolidin-2-one ring of rolipram (1) can be replaced by a 4,4-dimethyl-substituted pyrazolone ring (2) in a scaffold-hopping step, as was reported previously.[1a]

The early hit optimization program proceeded without structural information, and the heterocycle of 2 was decorated by N-alkylation, leading to isopropyl analog 3 with similar affinity (Table S2). We obtained the co-crystal structures of both 2 and 3 with hPDE4D (Figure 1, Table S6) as part of the current study. For compound 2, the dimethyl substituent of the pyrazolone ring faces the solvent-accessible space, while the nitrogen atoms interact with the water molecules surrounding the catalytic metal ions of the enzyme. This binding mode suggests that N-alkylation is not feasible, fortunately, introduction of N-alkyl substituents leads to a flip of the orientation of the pyrazolone ring. In the binding mode of 3, the dimethyl substituents are facing the water network around the metal ions, and the isopropyl substituent is directed to the solvent and interacts with the hydrophobic regions formed by (i) Phe340$^{S.35}$ and Met357$^{S.40}$; and (ii) Met273$^{MB1.17}$, Phe372$^{HC.52}$ and to a lesser extent Ile376$^{HC2.55}$ (Figure S3). Further optimization of the N-alkyl substituent resulted in the N-cycloheptyl analog 4. This aliphatic ring interacts more fully with the surrounding hydrophobic regions and leads to improved potency and affinity. The binding mode of 3 and 4 is comparable, except for the orientation of the O-cyclopentyl moiety that needs to adjust slightly to fit the binding site. This optimized cycloheptyl-substituted pyrazolone group was kept constant, while the other side of the molecule was grown in the direction of the Q2 pocket (in this region, the parasite TbrPDEB1 enzyme has the P-pocket, Figure S2).[2] Different 3-alkoxy substituents were introduced, including a flexible linker that contains a terminal phenyltetrazole moiety. This particular substituent works well in an alternative PDE inhibitor series, and is present in phthalazinone NPD-001 (Figure S1), the most potent TbrPDEB1 inhibitor reported to date.[16] In the pyrazolone series, this modification also leads to the most potent inhibitor (5, VUF13525). In both the phthalazinone and the pyrazolone series, this flexible tail did not reach the P-pocket but attained an aromatic stacking interaction with the sidechain of Tyr375$^{HC2.54}$ located outside of the catalytic site.[1c] This conformation maximizes hydrophobic interactions between the phenyltetrazole-containing moiety and Phe372$^{HC.52}$, Ile376$^{HC2.55}$, Met357$^{S.40}$ of the protein and with the N-cycloheptyl substituent of the ligand itself, thereby representing a hydrophobic collapse. As a result, 5 is a potent inhibitor of both hPDE4 and TbrPDEB1. It is noted that the low LLE of this series also reflects the high hydrophobicity of this class of compounds. To study the binding characteristics of the pyrazolones, an analogous compound with reduced potency and affinity (compound 6) was included as a negative control. This ligand contains a shorter and more rigid tetrazole-substituted moiety and cannot attain the stacking interaction with the Tyr375$^{HC2.54}$ residue. Instead, the tetrazole of 6 binds between a slightly hydrophilic region in helix 15 and the hydrophobic Met357$^{S.40}$ residue without forming any other polar interactions (Figure S4).

The thermodynamic hPDE4D binding profiles of 2 and 3 (Figures 2a and S5, Table S3) were obtained by modifying an isothermal titration calorimetry (ITC) protocol originally reported to assess rolipram (1) binding to hPDE4B.[17] The Gibbs energy ($\Delta G = -9.30$ kcal mol^{-1}, $K_D = 153$ nM) of 2 binding to the hPDE4D catalytic domain is dominated by a sizable enthalpic term ($\Delta H = -11.91$ kcal mol^{-1}) and an adverse entropic contribution ($-T\Delta S = 2.61$ kcal mol^{-1}). The introduction of the isopropyl substituent in 3 leads to inversion of the entropic term ($-T\Delta S = -2.44$ kcal mol^{-1}) that now contributes favorably to the overall interaction ($\Delta G = -9.60$ kcal mol^{-1}, $K_D = 91$ nM), with a reduced enthalpic contribution ($\Delta H = -7.16$ kcal mol^{-1}). While it is challenging to establish detailed STRs,[18] it is interesting to note that changes in thermodynamic profiles of close analogs can sometimes be attributed to differences in ligand binding modes (e.g., the flipping of a ring), as was also found in other studies such as a fragment optimization study with the acetylcholine binding protein (AChBP).[19]

The thermodynamic profiles of 5 and 6 (Figures 2a and S5, Table S3) were also obtained. The binding of 5 is driven by a sizable enthalpic term ($\Delta H = -11.38$ kcal mol^{-1}) and a small entropic term ($-T\Delta S = 0.32$ kcal mol^{-1}), indicating tight binding ($\Delta G = -11.06$ kcal mol^{-1}, $K_D = 8$ nM) to hPDE4D. The negative control, compound 6, demonstrated only 10-fold weaker binding ($\Delta G = -9.69$ kcal mol^{-1}, $K_D = 79$ nM), with a thermodynamic profile comparable to 5.

The target binding kinetics of this series was assessed using surface plasmon resonance (SPR)-biosensor assays. The previously reported SPR-based assay uses a capture-coupling protocol with His-tagged PDEs on NTA sensor chips.[20] However, the stability of this particular surface is not sufficient to accurately determine kinetic profiles. To this end, we developed an avidin-based immobilization protocol that can be used to capture biotinylated PDEs (see Experimental Section). These assay conditions led to stable surfaces that are sensitive enough to measure inhibitor binding kinetics.

Compounds 1–3 are well-behaved in the SPR biosensor assay, i.e., binding is fully reversible and data can be fitted to a 1:1 interaction model (Figure 2b, Table S2). The equilibrium dissociation constant of 1 ($K_D = 195$ nM) at the hPDE4D catalytic domain is comparable to values reported in literature (i.e., hPDE4D7 IC$_{50} = 288$ nM).[21] The association ($k_a = 1.01 \times 10^6$ M^{-1} s^{-1}) and dissociation ($k_d = 0.196$ s^{-1}) rate constants indicate that 1 has fast binding kinetics. Scaffold-hopping from the pyrrolidin-2-one ring of 1 to the pyrazolone ring of 2 resulted in a higher affinity ($K_D = 85$ nM) for hPDE4D, primarily

ChemMedChem

Research Article
doi.org/10.1002/cmdc.202400417

Chemistry Europe
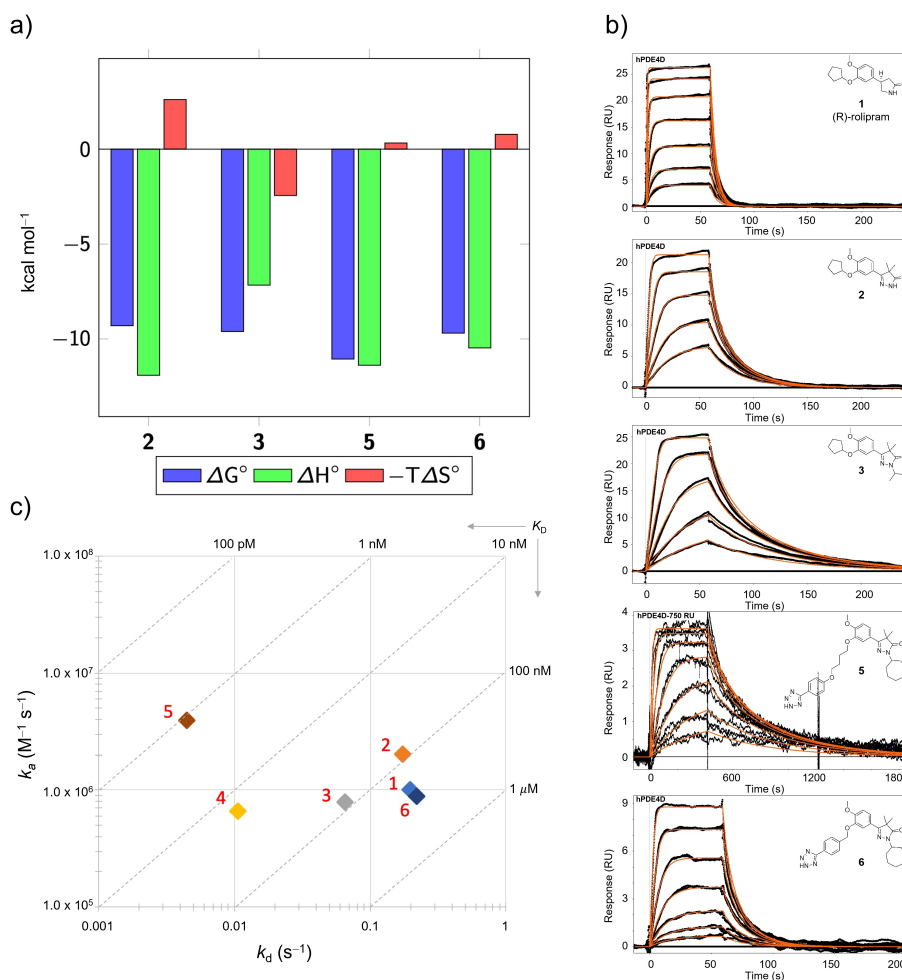European Chemical
Societies Publishing

Figure 2. Binding thermodynamics and kinetics of selected pyrazolone PDE inhibitors. a) Thermodynamic hPDE4D binding profiles of the following pairs: **2** and **3**; **5** and **6**. b) SPR sensorgrams at hPDE4D for **1–3**, indicating increasingly slower dissociation kinetics, and for **5** and **6**, highlighting a substantial difference in the binding affinity and kinetics, black curves represent the recorded data including repeated injections of each concentration, orange curves represent the 1:1 interaction model fitted on the sensorgrams, response in resonance units (RU) and time in seconds, representative sensorgrams for all compounds can be found in Table S5. c) SPR-derived kinetic rate plot for **1–6** at hPDE4D, with diagonals representing ligand affinity.

the result of an increased association rate ($k_a = 2.02 \times 10^6$ M^{-1} s^{-1}), and a slightly smaller dissociation rate ($k_d = 0.172$ s^{-1}) constant. The affinity of N-isopropyl analog **3** ($K_D = 83$ nM) is similar to its unsubstituted parent. However, the association ($k_a = 7.90 \times 10^5$ M^{-1} s^{-1}) and dissociation rate ($k_d = 0.0653$ s^{-1}) constants of **3** are smaller than those observed for **2**, providing an example of two compounds with similar K_D and ΔG values but varying kinetic and thermodynamic profiles.

The SKR of this series primarily indicates effects on the dissociation rate constant, while the association rate constant remains broadly comparable between compounds (Figure 2c, Table S2). The biosensor-derived affinities agree well with the biochemical PDE inhibition data (Table S1). The isopropyl/cyclo-heptyl substituent is the only difference between **3** and the 5-fold more potent **4** ($K_D = 16$ nM), representing an example of affinity gain by adding lipophilic bulk in permitted regions. In this case, the increase in affinity is primarily explained by a 6-fold decrease of the dissociation rate constant (Figure 2c, Tables S2 and S5). In the case of compound **5**, tight binding

and mass transfer effects warranted low protein immobilization levels and careful analyses. The relatively high association rate of **5** coupled to slow dissociation kinetics resulted in the highest-affinity hPDE4D interaction ($K_D = 1.14$ nM) of this series (Figure 2b, c, Table S2). The binding kinetics of the negative control **6** ($K_D = 249$ nM) are much faster, and its interaction with hPDE4D is 200-fold weaker than that observed for **5** (Figure 2b, c, Table S2). This finding agrees with the biochemical assay, where **6** showed a 100-fold lower potency than **5** (Table S1). However, the ITC-derived affinity of compound **6** differed only 10-fold from **5** (Table S3), and this discrepancy needs to be considered when directly comparing compounds and orthogonal methods.

The hPDE4 enzymes are well-studied proteins for which several biochemical and biophysical assays have been reported.[21–22] We have observed that similar studies with TbrPDEB1 are more challenging due to the lower stability of the expressed protein. However, we were able to obtain critical high-resolution structural (Table S7) and binding kinetics data

ChemMedChem

Research Article
doi.org/10.1002/cmdc.202400417

Chemistry
Europe
European Chemical
Societies Publishing

for several compounds. The overall protein structure of TbrPDEB1 is similar to hPDE4D (RMSD = 1.43 Å for the complexes bound to **3**). The immediate binding site shows an even higher similarity (RMSD = 0.38 Å for the residues within 6 Å of **3**). Although more water molecules are observed in the binding site of TbrPDEB1, other features are quite similar (Figure 3a). The interactions of **3** and **4** with TbrPDEB1 closely resemble those observed in hPDE4D (Figure 3b, c), although the cyclopentyloxy-substituent of **3** adopts a slightly different conformation in TbrPDEB1. The binding mode of **5** in TbrPDEB1 is also highly similar (Figure 3d). However, the geometry of the stacking interaction of the phenyltetrazole moiety with Phe880$^{HC2.54}$ in TbrPDEB1, compared to Tyr375$^{HC2.54}$ in hPDE4D, seems to be suboptimal, possibly indicating a smaller contribution to the binding of **5** to TbrPDEB1. The parasite-specific P-pocket was not targeted by any compound in this series.

The SPR biosensor assay did not allow high enough concentrations of **1** and **4** to measure binding at TbrPDEB1, while **2** ($K_D = 18.5$ μM) and **3** ($K_D = 14.6$ μM) interacted more than 100-fold weaker with TbrPDEB1 than with hPDE4D (Table S4). In addition to the standard multicycle experiment (Table S5), the binding kinetics of **5** at TbrPDEB1 were also

determined with a single-cycle assay (Figure S6), a time-efficient method allowing complete kinetic profiling, and indicated a 40-fold lower affinity ($K_D = 43.5$ nM, Table S4) when compared to hPDE4D (Figure 3e). This substantial drop in affinity resulted from changes in the association ($k_a = 4.28 \times 10^5$ M^{-1} s^{-1}) and the dissociation ($k_d = 1.86 \times 10^{-2}$ s^{-1}) rate constants. The binding affinity of **6** ($K_D = 469$ nM, Table S4, Figure S6) was 2-fold lower than on hPDE4D, fully explained by a change in dissociation rate constant (Figure 3e).

For the TbrPDEB1-inhibitor discovery program, the high hPDE4 potency of compound **5** was undesirable. The structural data obtained in the current study indicates similar binding modes in both TbrPDEB1 and hPDE4D without offering sufficient insights to explain the higher affinity for the human target. However, the binding kinetics do reveal interesting differences that were further explored by computational studies. *In silico* evaluation of kinetic parameters using unbiased molecular dynamics (MD) is far from trivial, as it requires extensive sampling, and MD calculations are often limited to a microsecond timescale. In contrast, ligand dissociation can take minutes or even hours. Hence, we applied biased MD methods to study unbinding *in silico*. In these simulations, a bias factor is
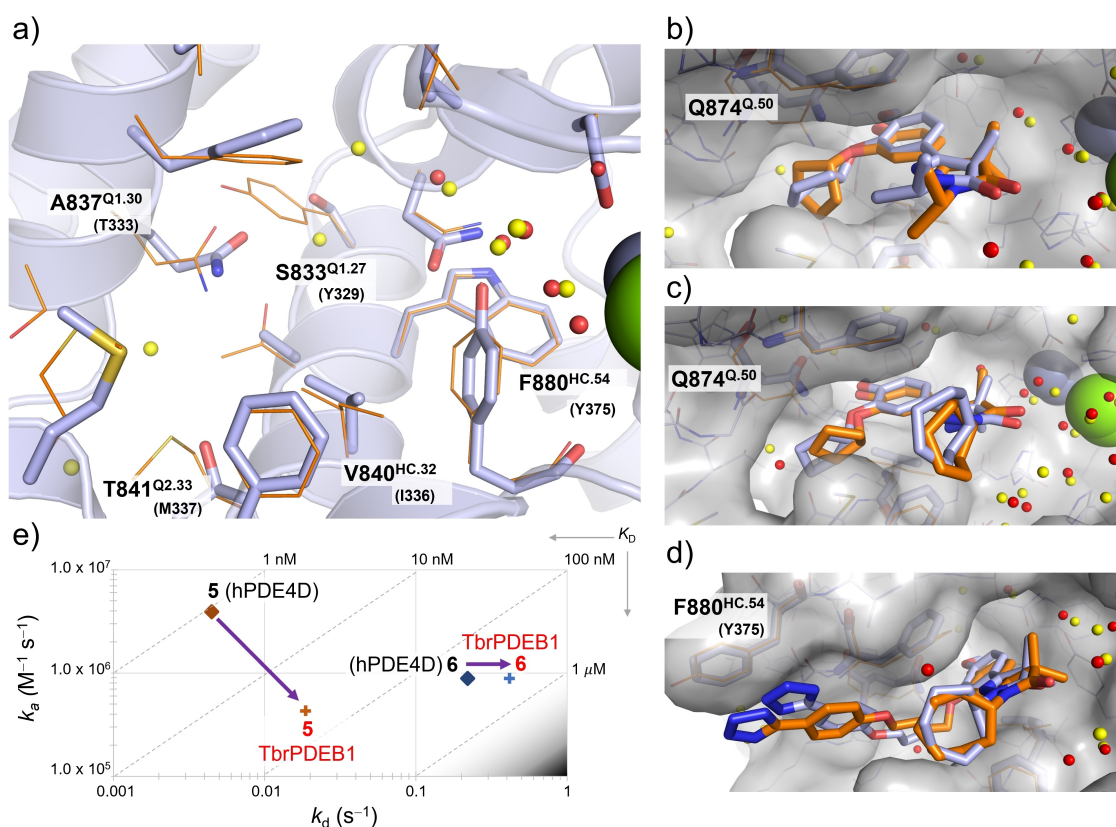

Figure 3. Interaction of pyrazolone inhibitors with TbrPDEB1. Binding site alignments of TbrPDEB1 (blue) and hPDE4D (orange) based on X-ray crystal structures, nonidentical residues are labeled with the corresponding hPDE4D residue code shown between parenthesis, yellow and red spheres denote TbrPDEB1 and hPDE4D binding site water molecules, respectively, the magnesium and zinc cations are displayed as gray and green spheres, respectively, all panels are rendered with Gln$^{Q.50}$ on the left and the metal ions on the right side of the panel. a) Binding site comparison of the inhibitor-bound protein conformation based on the co-crystal structures of **3** (ligand omitted for clarity). In the other panels, TbrPDEB1 is shown as a gray surface, key TbrPDEB1 (blue) residues are shown as sticks, and key hPDE4D (orange) residues are shown as lines, with the following co-crystallized ligands: b) **3**; c) **4**; d) **5**. e) SPR-derived kinetic rate map, with arrows starting in the hPDE4D-data point indicating the shift in target binding kinetics at TbrPDEB1. Representative sensorgrams can be found in Table S5 and Figure S6. The position of low affinity compounds **2** and **3** on the kinetic rate map cannot be accurately determined, and this is indicated with a gray-to-black gradient in the bottom right corner.

ChemMedChem

Research Article
doi.org/10.1002/cmdc.202400417

Chemistry Europe
European Chemical
Societies Publishing

applied to the system to promote inhibitor unbinding, shorten simulation time and improve sampling.

To assess whether the hydrogen bond between $Gln^{Q.50}$ and the inhibitors plays a role, we applied dynamic undocking (DUck),[23] a steered MD (SMD) simulation protocol, to the co-crystal structures. Essentially, this method interrogates the strength of this hallmark hydrogen bond by determining the work needed to reach a quasi-bound state (W_{QB}) of the PDE-inhibitor complex (Figure 4a, b).[23] In this particular simulation, the selected intermolecular hydrogen bond with $Gln^{Q.50}$ is pulled from an initial distance of 2.5 Å (hydrogen-bonded state) to 5.0 Å (quasi-bound state) while W_{QB} is computed. Simulations were run to estimate W_{QB} for individual hydrogen bonds to the central 3,4-dialkoxyphenyl oxygen atom O1 or O2 (Figure 4c) in all co-crystal structures. The W_{QB} values were calculated for 100 trajectories per complex and the results indicate that hydrogen bonds were consistently stronger in hPDE4D than in TbrPDEB1

(Table S8). Furthermore, the hydrogen bond formed with O1 was stronger than with O2 for most complexes (Table S9). Therefore, we assume the hydrogen bond with O1 is most critical in the dissociation of this series. The minimum W_{QB} for O1 is higher for **3** and **5** in hPDE4D than in the corresponding TbrPDEB1 complexes (Figure 4d). Together these results indicate a higher stability of the hPDE4D-inhibitor complex, but they are too subtle to explain the observed dissociation kinetics.

Therefore, we turned our attention to the study of unbinding with τ-random acceleration molecular dynamics (τRAMD) simulations. This protocol probes the whole unbinding process and explores a variety of possible ligand egress pathways.[24] For each protein-ligand complex, 50 trajectories were generated and the computational residence times (τ_{comp}) calculated (Figure 4e). The computed ligand egress pathways are diverse, especially in the later stages of unbinding, although
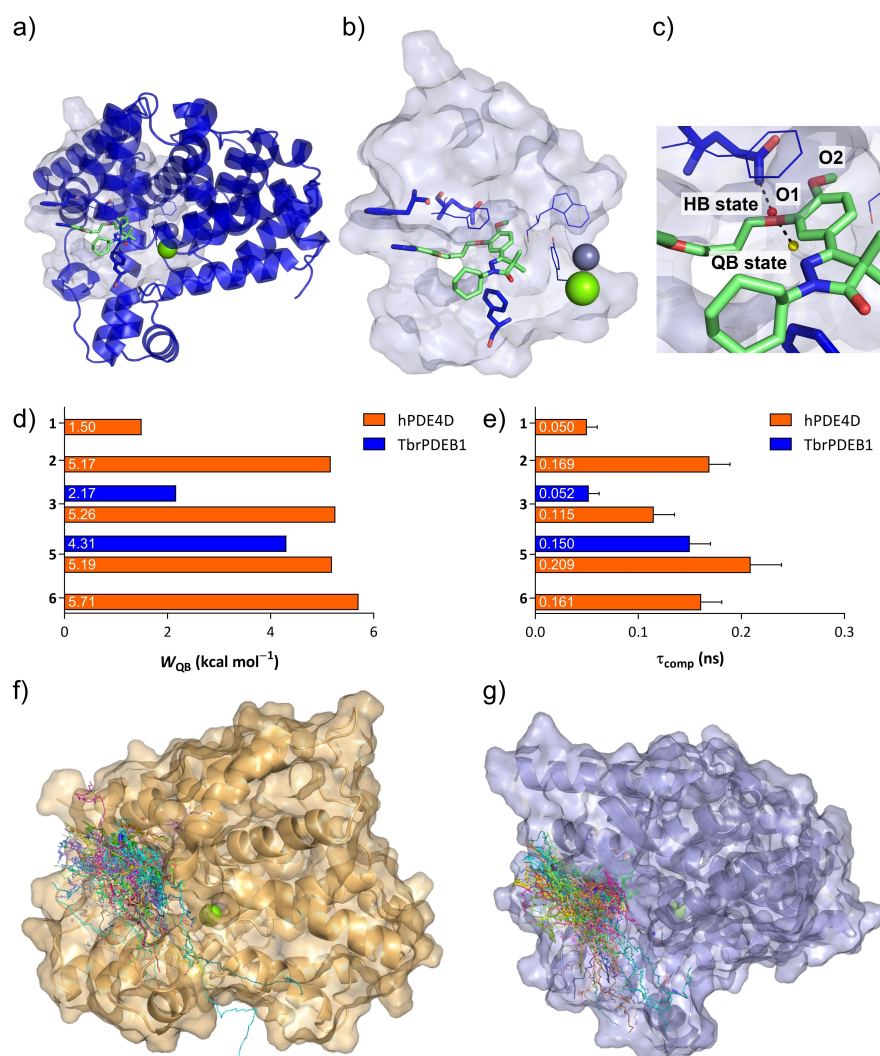

Figure 4. Interrogation of target-binding determinants with steered and random acceleration MD simulations. a) Overview of DUck simulation area relative to the full PDE catalytic domain. b) Surface representation of the DUck simulation area. c) Close-up representation of the hydrogen bond between $Gln^{Q.50}$ and O1 (O2 also indicated). d) Minimum W_{QB} values for O1 in hPDE4D (orange) and TbrPDEB1 (blue). e) Calculated residence times (τ_{comp}) for simulated hPDE4D (orange) and TbrPDEB1 (blue) co-crystal complexes in τRAMD simulations (mean values ± s.d.). f) and g) Overlay of all 50 egress pathways derived from τRAMD simulations for **5** with hPDE4D (orange) and TbrPDEB1 (blue).

ChemMedChem

Research Article
doi.org/10.1002/cmdc.202400417

Chemistry
Europe
European Chemical
Societies Publishing

in hPDE4D (Figure 4g), the directionality of egress is slightly more uniform than in TbrPDEB1 (Figure 4f). The τ_{comp} values, derived from the trajectories and calculated using a statistical bootstrapping step (Table S10), do not fully reproduce the compound ranking observed in the SPR biosensor assay. However, in line with the SPR data, **1** was the compound with the shortest residence time, and **5** had the longest residence time (Figure 4e). It is also noted that this method predicts the faster dissociation of compound **6**, which is used as a negative control that is structurally similar to **5**. Furthermore, the TbrPDEB1-inhibitor complexes formed with **3** and **5** are calculated to dissociate ~20% faster than the corresponding hPDE4D complexes (Figure 4e), and this agrees with the SPR data.

The obtained trajectories offer a well-sampled dataset to study the contacts during the simulated unbinding process. For this, interaction fingerprint (IFP) analyses were performed on all the τRAMD trajectories that were generated for **5** with both hPDE4D (Figure 5a) and TbrPDEB1 (Figure 5b). Analysis of the contacts between either protein and **5** confirms that the interaction with the anchoring Gln$^{Q.50}$ is more rapidly lost in the TbrPDEB1 complex. This agrees with the DUck simulations, indicating that rupturing this hydrogen bond in TbrPDEB1 is easier than in hPDE4D. To understand how the interaction is broken, the IFP analysis was extended to quantify water-mediated interactions between Gln$^{Q.50}$ and **5**. IFPs derived from the τRAMD trajectories indicate that the frequency of water-

mediated interactions between Gln$^{Q.50}$ and compound **5** is substantially lower in hPDE4D (Figure 5d) than in TbrPDEB1 (Figure 5e), especially in the early phases of unbinding. This indicates that in TbrPDEB1, water molecules quickly start to interfere with the interaction between this critical residue and **5**. These results demonstrate the dynamic character of the water molecules around Gln874$^{Q.50}$ in TbrPDEB1 that facilitate the unbinding of **5**, thereby explaining faster complex dissociation.

To understand the role played by water molecules in the dissociation of these complexes, we studied the water molecules in proximity to Gln$^{Q.50}$. First, we performed a WATCLUST analysis on the τRAMD trajectories. WATCLUST is a method that identifies water clusters in MD simulation data.[25] For the TbrPDEB1 unbinding simulations, WATCLUST reveals a water network that extends from the P-pocket towards the back of the Gln874$^{Q.50}$ side chain (Figure 6b). Furthermore, the properties of these water molecules were characterized by WaterFLAP[26] and the water molecules near Gln874$^{Q.50}$ have bulk-like characteristics that form a channel to those in the solvent-accessible P-pocket (Figure 7b). This water channel is not present in the hPDE4D binding site (Figure 6a and 7a), providing further support to the notion that the water molecules in TbrPDEB1 help drive complex dissociation.

Biophysical assays have provided detailed information on the structures and binding kinetics of the pyrazolone PDE inhibitors. The computational studies indicate a well-defined
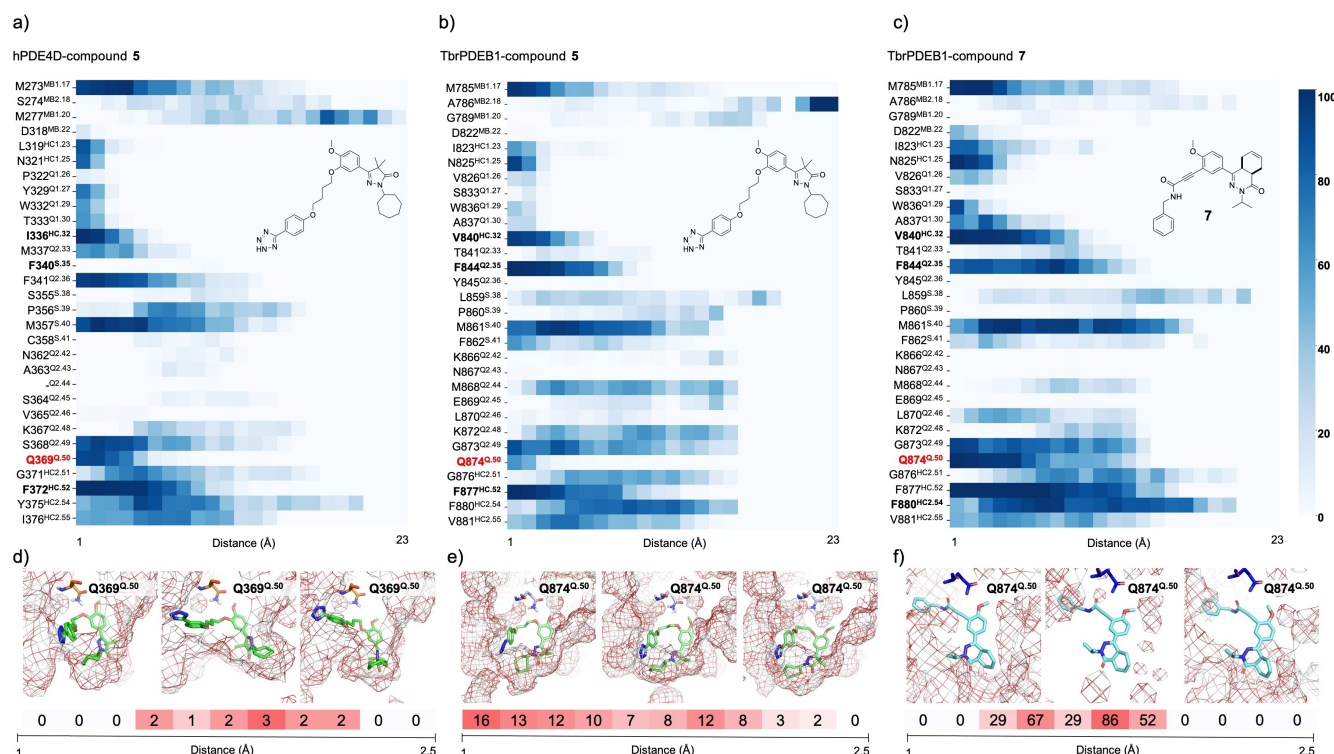

Figure 5. Contact analysis of ligand egress pathways derived from τRAMD simulations. Direct protein-ligand contact heatmaps of a) hPDE4D-**5**; b) TbrPDEB1-**5**; and c) TbrPDEB1-(4a*R*,8a*S*)-**7** (PDB code: 6GXQ), with Gln$^{Q.50}$ (red) and the hydrophobic clamp residues highlighted in bold font, heatmap intensity colored according to the scale (blue gradient) shown on the right representing the percentage of direct contacts observed with the distance (in Å) calculated during the ligand egress pathway. Water-density contour and water-IFP heatmap analysis of the following complexes: d) hPDE4D-**5**; e) TbrPDEB1-**5**; and f) TbrPDEB1-(4a*R*,8a*S*)-**7**, with the occurrence of water-Gln$^{Q.50}$ interactions as a normalized number at the indicated distance (in Å).
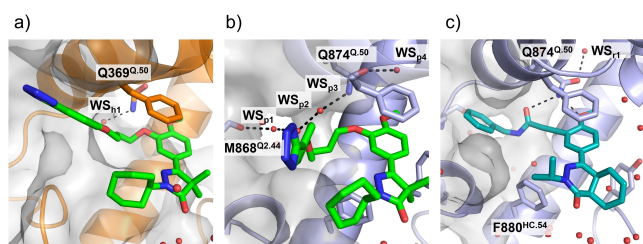
ChemMedChem

Research Article
doi.org/10.1002/cmdc.202400417

Chemistry Europe
European Chemical
Societies Publishing

Figure 6. WATCLUST analysis of the τRAMD trajectories of a) **5**-hPDE4D; b) **5**-TbrPDEB1; and c) (4a*R*,8a*S*)-**7**-TbrPDEB1 (PDB code: 6GXQ). Water clusters are shown as red spheres, and water clusters interacting with Gln$^{Q.50}$ are labeled and connected with a dashed line.
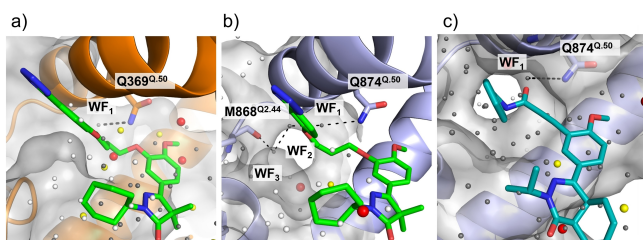

Figure 7. WaterFLAP analysis of compound **5** in hPDE4D (a) and TbrPDEB1 (b), and compound (4a*R*,8a*S*)-**7** in TbrPDEB1 (PDB code: 6GXQ) (c). Color-coding of the calculated waters and predicted energies: red ($\Delta G > 3.5$ kcal mol^{-1}), yellow (ΔG between 2.0 and 3.5 kcal mol^{-1}), gray (ΔG between -1.0 and 2.0 kcal mol^{-1}), and blue ($\Delta G < -1.0$ kcal mol^{-1}). The water network extending from Gln$^{Q.50}$ towards the Q2 pocket (hPDE4D) or P-pocket (TbrPDEB1) is indicated with a black dashed line and labeled.

Figure 8. Profile of phthalazinone-alkynamide **7**. a) Structure, affinity and LLE of **7**, K_D values are derived from the kinetic analysis of SPR biosensor data. b) Sensorgrams of **7** binding to hPDE4D (top) and TbrPDEB1 (bottom), black curves represent the recorded data including repeated injections of each concentration, orange curves represent the fitted 1:1 interaction model, response in resonance units (RU) and time in seconds.

water channel connecting bulk water via the parasite-specific P-pocket towards the critical residue Gln$^{Q.50}$, leading to faster inhibitor unbinding in TbrPDEB1 than in hPDE4D. There is no water channel or P-pocket in hPDE4D, thus the anchoring hydrogen bond with Gln$^{Q.50}$ is more shielded from water. The recently published phthalazinone-alkynamide TbrPDEB1 inhibitors[27] represent an interesting case study. These phthalazinones were also optimized by growing towards the P-pocket. The main compound of this series, NPD-1335 (**7**, Figure 8a), has been reported to have a slightly higher activity against TbrPDEB1 ($K_i = 158$ nM) than against hPDE4B ($K_i = 794$ nM), and was found to bind with similar affinity ($K_D = 79$ nM) to both targets.[27] The SPR biosensor analysis reveals that this compound has an improved kinetic profile as it dissociates slower from TbrPDEB1 (Figure 8c) than from hPDE4D (Figure 8b). The application of the computational analyses described above to (4a*R*,8a*S*)-**7** indicate that the amide carbonyl of **7** disrupts the TbrPDEB1 water channel (Figure 6c and 7c). This leads to prolonged and more frequent interactions between the ligand and Gln$^{Q.50}$ (Figures 5c and S7). IFP analysis of water-mediated interactions in TbrPDEB1 confirms that the water molecules that rapidly get in-between pyrazolone **5** and Gln874$^{Q.50}$ are not as efficient in driving the unbinding of **7** (Figure 5f), explaining slower TbrPDEB1 dissociation kinetics and a more favorable selectivity profile. These findings demonstrate that disrupting the water channel in TbrPDEB1 and shielding the critical inhibitor-Gln874$^{Q.50}$ hydrogen bond is a viable design strategy, and that this concept is applicable to inhibitors, such as **7**, that
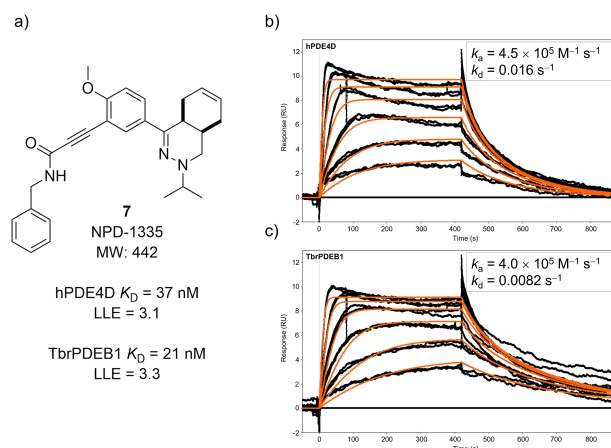
target the P-pocket. Our studies also confirm the importance of water molecules in residence time, as also recognized by others.[28] The molecular understanding that results from the combination of biophysical and computational studies can help to design better ligands.

Conclusions

Our structural, biophysical, and computational investigations indicate several molecular features contributing to the target binding kinetics and selectivity of pyrazolone PDE inhibitors. The displacement of an anchoring hydrogen bond by a water molecule is critical in PDE-inhibitor complex dissociation. In TbrPDEB1, the intervening water molecule is connected to the parasite-specific P-pocket via a well-defined water channel, and these water molecules have bulk-like characteristics. This contributes to faster inhibitor dissociation in TbrPDEB1, while in hPDE4D, the same hydrogen bond is less prone to displacement, thereby explaining slower dissociation. Designing compounds that interrupt this water channel is a viable strategy towards more selective TbrPDEB1 inhibitors. Our computer-aided drug design protocols can be used to explain, introduce or optimize kinetic selectivity. Furthermore, this approach can also be applied to the discovery of PDE inhibitors against other major parasites, as it has been shown that a similar P-pocket is also present in the PDEs of related parasites, such as *Leishmania major* PDE B1 (LmjPDEB1) and *T. cruzi* PDE C (TcrPDEC).[1b]

ChemMedChem

Research Article
doi.org/10.1002/cmdc.202400417

Chemistry Europe
European Chemical
Societies Publishing

Experimental Section

Chemistry

All reagents and solvents were obtained from commercial suppliers and were used as received. All reactions were magnetically stirred and carried out under an inert atmosphere. Reaction progress was monitored using thin-layer chromatography (TLC) and LC–MS analysis. Silica gel column chromatography was carried out manually or with automatic purification systems using the indicated eluent. Nuclear magnetic resonance (NMR) spectra were recorded on a Bruker Avance 500 (500 MHz for ^{1}H and 126 MHz for ^{13}C) instrument equipped with a Bruker CryoPlatform. Chemical shifts (δ in ppm) and coupling constants (J in Hz) are reported with residual solvent as internal standard (δ ^{1}H NMR: CDCl$_3$ 7.26; DMSO-d_6 2.50; δ ^{13}C NMR: CDCl$_3$ 77.16; DMSO-d_6 39.52). LC–MS analysis was performed on a Shimadzu LC-20AD liquid chromatograph pump system, equipped with an Xbridge (C18) 5 μm column (50 mm, 4.6 mm), connected to a Shimadzu SPD–M20 A diode array detector, and MS detection using a Shimadzu LC–MS-2010EV mass spectrometer. The LC–MS conditions were as follows: solvent B (acetonitrile with 0.1% formic acid) and solvent A (water with 0.1% formic acid), flow rate of 1.0 mL/min, start 5% B, linear gradient to 90% B in 4.5 min, then 1.5 min at 90% B, then linear gradient to 5% B in 0.5 min, then 1.5 min at 5% B; total run time of 8 min. Exact mass measurement (HRMS) was performed on a Bruker micrOTOF–Q instrument with electrospray ionization (ESI) in positive ion mode and a capillary potential of 4,500 V. Systematic names for molecules were generated with ChemBioDraw Ultra 14.0.0.117 (PerkinElmer, Inc.). The reported yields refer to isolated pure products; yields were not optimized. The purity, reported as the peak area % at 254 nm, of all final compounds was $\geq$95% based on LC–MS.

Synthetic Procedures

Compounds **2**, **4–6** and building block **8** were prepared as previously described.[1a] Compound **7** was prepared as previously described.[27]
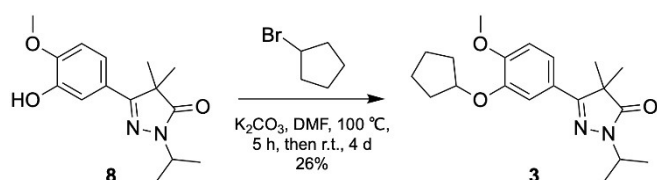
5-(3-(Cyclopentyloxy)-4-methoxyphenyl)-2-isopropyl-4,4-dimethyl-2,4-dihydro-3H-pyrazol-3-one (3)

To a solution of building block **8** (140 mg, 0.50 mmol) in DMF (7.5 mL) was added K$_2$CO$_3$ (158 mg, 1.14 mmol) and bromocyclopentane (0.1 mL, 1.14 mmol). The reaction mixture was heated to 100 °C for 5 h, and stirred at r.t. until TLC indicated full conversion (after 4 d). Water (20 mL) and Et$_2$O (20 mL) were added. The organic phase was collected and the aqueous phase was extracted with Et$_2$O (3×50 mL). The combined organic layers were washed with 1 M NaOH (50 mL), water (50 mL), brine (50 mL) and concentrated *in vacuo*. The crude product was purified by automatic flash column chromatography (Biotage KP-Silica 25 g) eluting with CH$_2$Cl$_2$/MeOH 99:1, to provide title compound **3** as a white solid (47 mg, 26% yield). TLC: R_F = 0.3 (CH$_2$Cl$_2$/MeOH 99:1). ^{1}H NMR (500 MHz, CDCl$_3$) δ 7.42 (d, J = 1.9 Hz, 1H), 7.30 (dd, J = 8.4, 1.9 Hz, 1H), 6.86 (d, J = 8.4 Hz, 1H), 4.84 (tt, J = 6.3, 3.3 Hz, 1H), 4.50 (hept, J = 6.7 Hz, 1H), 3.88 (s, 3H), 2.03–1.81 (m, 6H), 1.68–1.60 (m, 2H), 1.46 (s, 6H), 1.36

(d, J = 6.7 Hz, 6H). ^{13}C NMR (126 MHz, CDCl$_3$) δ 178.0, 161.6, 151.6, 147.9, 124.1, 119.4, 112.5, 111.3, 80.7, 56.1, 49.0, 45.3, 33.0, 24.4, 23.0, 20.9. LC–MS (ESI): t_R = 5.60 min, area: 98% (254 nm), m/z 345 [M+H]$^+$. HRMS (ESI) m/z: calcd for C$_{20}$H$_{29}$N$_2$O$_3$ [M+H]$^+$ 345.2167, found 345.2173.

Interference Compounds

All compounds utilized in this study have been examined for the presence of substructures classified as Pan Assay Interference Compounds (PAINS) using a KNIME workflow.[29]

Gene Constructs for Structural Studies

Gene constructs for production of hPDE4D2 and TbrPDEB1 catalytic domain proteins were designed as previously described.[1c] Gene segments coding for hPDE4D2 catalytic domain (residues 381–740) and TbrPDEB1 catalytic domain (residues 565–918) were cloned into a pET15b and pET28a(+) E. coli expression vectors respectively. In both cases, a vector supplied, N-terminal 6×His tag was kept in-frame with the target protein to facilitate purification by metal affinity chromatography.

Protein Expression and Purification

hPDE4D2 and TbrPDEB1 catalytic domain proteins used in this study were expressed and purified as previously described.[1c] Briefly, the proteins were expressed in E. coli host cells and subsequently purified by Ni-NTA metal affinity, ion exchange and size exclusion chromatography techniques to crystallization grade purity. The N-terminal 6×His tag of the proteins was removed prior to their use in crystallization.

Protein Crystallization, Ligand Soaking and Data Collection

Apo crystals of hPDE4D2 and TbrPDEB1 catalytic domains were grown in 24 well XRL plates (Molecular Dimensions, Newmarket, Suffolk, UK) by the vapor diffusion hanging drop technique. Typically, protein and crystallization solutions were mixed in 1:1 ratio, and drops were set up against a 500 μL reservoir solution. Crystals of hPDE4D were obtained in a condition containing 24% PEG 3350, 30% ethylene glycol and 100 mM HEPES pH 7.5 at 19 °C and soaked with different inhibitors to obtain protein-inhibitor complexes. TbrPDEB1 crystals obtained in a condition containing 20% PEG 3350, 400 mM sodium formate, 300 mM guanidine and 100 mM MES pH 6.5 at 4 °C were complexed with inhibitors in a similar way. The soaking duration for inhibitors varied from over-night to 48 hours. The soaked crystals were then cryo-protected, mounted on CryoLoop (Hampton Research, Aliso Viejo, CA, USA) or LithoLoops (Molecular Dimensions, Sheffield, UK) and vitrified in liquid nitrogen prior to data collection. All X-ray diffraction data sets were collected at Diamond Light Source (DLS; Didcot, Oxfordshire, UK) at beamline I03 using a Pilatus 6 M detector (Dectris, Baden, Switzerland) or at beamlines I04 and I04-1 using a Pilatus 6M–F detector (Dectris, Baden, Switzerland) at 100 K temperature. The data sets were processed by xia2[30] or autoPROC[31] data processing pipelines, which incorporate XDS[32] and AIMLESS[33] for data reduction and scaling, and are available at DLS.

X-ray Crystal Structure Determination, Refinement and Analysis

Structures of inhibitor complexes with hPDE4D2 and TbrPDEB1 were determined by molecular replacement in CCP4 suite[34]

ChemMedChem

Research Article
doi.org/10.1002/cmdc.202400417

Chemistry
Europe
European Chemical
Societies Publishing

program PHASER[35] by using the respective apo models (hPDE4D2, PDB code: 3SL3; TbrPDEB1, PDB code: 4I15) as search templates. Stereochemical restraints for the inhibitors were generated by ACEDRG available within the CCP4 package[34] or with the Grade Web Server (http://grade.globalphasing.org/). Adjustment of the models, as well as ligand fitting, was performed with COOT[36] and refinement was performed with REFMAC5.[37] The final structures had good geometry and could be refined to low R-factors (Tables S6 and S7). All refined models were validated with MOLPROBITY.[38] Data collection and refinement statistics are given in Tables S6 and S7. Root-mean-square (r.m.s.) deviation values were calculated from a sequence alignment, structural super-position and refinement cycle on Cα carbons with the align function as implemented in PyMOL 2.5.2 (Schrödinger, LLC). Residue numbers were derived from crystal structures; residues have been labeled according to the PDEStrIAn nomenclature system (http://pdestrian.vu-compmedchem.nl/).[2] Structural figures were prepared with PyMOL 2.5.2. For clarity, selected residues from the helix capping the substrate-binding pocket (i.e., D784, M785, A786, K787, H788, G789, S790, A791, L792, E793 in TbrPDEB1; D272, M273, S274, K275, H276, M277, N278, L279 in hPDE4D) have been omitted in the rendering of the main-text figures. Coordinates of the structures have been deposited to the RCSB Protein Data Bank with following accession codes: 7ABD (hPDE4D2-**2**, NPD-768); 7ABJ (hPDE4D2-**3**, NPD-1361); 7ABE (hPDE4D2-**4**, NPD-769); 7AAG (hPDE4D2-**5**, NPD-617 [VUF13525]); 7 A8Q (hPDE4D2-**6**, NPD-654); 6QGU (TbrPDEB1-**3**, NPD-1361); 6QGP (TbrPDEB1-**4**, NPD-769); and 7 A28 (TbrPDEB1-**5**, NPD-617 [VUF13525]).

PDE Activity Assay

To determine the effect of test compounds on the enzymatic activity of full-length TbrPDEB1 ($K_m = 7.97 \pm 2.32\ \mu M$) and full-length recombinant hPDE4B1 ($K_m = 2.0 \pm 0.7\ \mu M$), the standard scintillation proximity assay (SPA) was used, as reported previously.[1a,39] In this assay, the cAMP substrate concentration was 0.5 μM, and the enzyme concentration was adjusted so that < 20 % of substrate was consumed. The pK_i values are the mean of at least two independent experiments.

Isothermal Titration Calorimetry

The untagged catalytic domains of hPE4D2 and TbrPDEB1 were dialyzed in 10 mM HEPES (pH 7.4), 150 mM NaCl, 2 mM 2-mercaptoethanol, 2 mM MgCl₂, 100 nM ZnCl₂ using Slide-A-Lyzer 10 K MWCO dialysis cassettes (Thermo Scientific) in two steps: (1) overnight at 4 °C against 2 L buffer; and (2) for 2–4 h against a freshly prepared 0.5 L buffer that was used to prepare the sample cell and syringe solutions with a final DMSO concentration of 2 % (v/v). Experiments were performed at 25 °C with a reference power of 10 μcal/s and a stirring speed of 1000 rpm using a MicroCal Auto-iTC200 instrument (Malvern). The ligand titration protocol included an initial 0.4 μL injection of 0.8 s that was discarded from the analysis, followed by (19×) 2 μL injections of 4 s, with a spacing of 150 s and a filter period of 5 s. The protein/ligand concentration ratio for each run was initially determined with $C = n \cdot [M]/K_D$ where [M] denotes the molar concentration in the sample cell; K_D the equilibrium dissociation constant; n the stoichiometry, with C in the 5–500 range. The heat of dilution was determined for ligands in separate titrations in buffer without protein, and was subtracted from the interaction data. The corrected interaction data were analyzed with Origin software provided by the manufacturer using a one-site binding model to obtain the equilibrium association constant (K_A), the enthalpy of binding (ΔH) and stoichiometry (n).

Surface Plasmon Resonance

All surface plasmon resonance (SPR)-based biosensor experiments were performed with a Biacore T200 instrument (GE Healthcare) using series S CM5 or SA sensor chips (GE Healthcare), and responses in resonance units (RU) were recorded real-time at 10 Hz. All solutions were freshly prepared, filtered, and degassed. Neutravidin in HBS–N was immobilized on CM5 sensor chips at a flow speed of 10 μL/min at 25 °C, the surface was activated for amine coupling using EDC/NHS (440 s), neutravidin (0.30 mg/mL) in a 10 mM NaAc solution (pH 5.0) was injected for 120 s, followed by the injection of ethanolamine HCl (1 M) for 420 s. The catalytic domains of hPDE4D2 and TbrPDEB1 were buffer-exchanged using Amicon Ultra 0.5 mL centrifugal filters (Merck) to HBS–N with 5 % glycerol (v/v), 4 μM MgCl₂·6 H₂O, 100 nM ZnCl₂, 2 mM 2-mercapto-ethanol and diluted to 1 mg/mL. EZ-Link Sulfo-NHS-Biotin (Thermo Fisher Scientific) was diluted to 1.5 mM in the same buffer, mixed with the protein in a 1:1 ratio, and incubated at 4 °C overnight. Biotinylated proteins were buffer-exchanged to 50 mM Tris-HCl (pH 8.0), 150 mM NaCl, 4 mM MgCl₂·6 H₂O, 100 nM ZnCl₂, 5 % glycerol (v/v), 2 mM 2-mercaptoethanol, and desalted using 0.5 mL Zeba Spin desalting columns (Thermo Scientific). Proteins were diluted to 100 μg/mL and injected on the flow channels until 2500– 4000 RU on neutravidin-functionalized CM5 sensor chips at 15 °C, followed by a biocytin (0.05 mg/mL) injection for 120 s on all flow channels at 15 °C. On SA sensor chips, proteins were immobilized to specific densities of 750 and 1500 RU. All compounds were dissolved in DMSO (stock solutions of 10 mM) and diluted (through one or more intermediate dilution steps) in 50 mM Tris-HCl (pH 8.0), 150 mM NaCl, 4 mM MgCl₂·6H₂O, 100 nM ZnCl₂, 5 % glycerol (v/v), 2 mM 2-mercaptoethanol, 0.005 % Tween-20 (v/v), the final concen-tration of DMSO was 2 % (v/v) in all experiments. Suitable concentration ranges and injection times were determined for each compound separately. All compound titrations were run at 25 °C at a flow speed of 50 μL/min. In multicycle experiments, a 7-point concentration range of each compound was measured in duplicate, and curves disrupted with obvious aberrant features were removed. Compounds **1–6** were injected for 60 s, and dissociation was monitored for 300 s on CM5 sensor chips. Compound **5** and **7** were injected for 420 s on SA sensor chips, dissociation was monitored for 2000 s and 900 s, respectively. Single-cycle experiments were performed for **5** using CM5 sensor chips and comprised five injections of 60 s followed by a dissociation period of 900 s. In all experiments, compounds **1** and NPD-1170[27] were used as refer-ence compounds; data obtained from CM5 and SA sensor chips were similar. Raw biosensor data was double referenced by subtracting reference channel and blank injection data, and solvent corrected. Steady-state affinity and kinetic analyses were performed with a 1:1 binding model, equilibrium-binding fits generally agreed with the K_D derived from kinetic fits, data and fits from multicycle experiments agreed with those from single-cycle experiments. Data derived from kinetic analyses were used to evaluate both affinity and structure-kinetics relationships except for TbrPDEB1-**2** and TbrPDEB1-**3**. Sensorgrams were analyzed using Biacore T200 evaluation software (version 2.0, General Electric Company) and Scrubber2 (version 2.0c, BioLogic Software); sensorgrams, kinetic and mass transport terms were further assessed using the BIAsimulation (version 2.1, Biacore AB) tool to verify that curves simulated with the experimental terms were comparable to the sensorgrams that were actually fitted. The final multicycle sensor-grams, data fits, and figures were produced with Scrubber2, and single-cycle sensorgrams were analyzed with standard Biacore evaluation software.

ChemMedChem

Research Article
doi.org/10.1002/cmdc.202400417

**Chemistry
Europe**
European Chemical
Societies Publishing

Dynamic Undocking Simulations

The dynamic undocking (DUck) simulations were performed on the co-crystal structures of hPDE4D with (R)-**1** (PDB code: 1Q9 M) and **2**--**6**; and TbrPDEB1 with **3** and **5**. The work (W_{QB}) needed to break the hydrogen bond (HB) between $Gln^{Q.50}$ and the ligand oxygen on the 3-position of the central 3,4-dialkoxyphenyl ring (O1) or the oxygen on the 4-position (O2) was obtained by running separated and independent simulations. The W_{QB} was calculated over a distance of 2.5 Å–5.0 Å according to the DUck protocol.[23] Residues within 8 Å of the target HB were extracted from the protonated protein to create a model protein chunk (simulation area) used as input. A scientific vector language (SVL) script was used to automate the calculation of AM1-BCC ligand charges, assignment of parm@Frosst atom types and non-bonded parameters to the ligand, writing of simulation input files, and execution of tleap to generate topology and coordinate files for each complex. The protein was parameterized using the Amber 99SB-ILDN force field and a TIP3P water model. All simulations were performed with AMBER 14 (University of California, San Francisco) with the work-flow and conditions as described.[23] The length of the MD step simulated between every SMD step was 0.5 ns. To ensure extensive sampling, each simulated interaction was run 50 times, each with two parallel simulations at 300 K and 325 K, respectively.

Random Acceleration Molecular Dynamics

The τ-random acceleration molecular dynamics (τRAMD) simulations of hPDE4D with (R)-**1** (PDB code: 1Q9 M), **2–6** and (4aR,8aS)-**7** (PDB code: 6HWO); and TbrPDEB1 with **3**, **5** and (4aR,8aS)-**7** (PDB code: 6GXQ) were performed analogously to the original protocol.[24] Ligand protonation states were assigned using MOE 2018.10 (Molecular Operating Environment, Chemical Computing Group), and ligand parameters were generated using the restrained electrostatic potential (RESP) method. The protein was protonated (pH 7.5) using AmberTools14 (University of California, San Francisco). The GAFF and Amber14 force fields were employed respectively for the ligands and the protein. The crystallographic water molecules within 8 Å from the ligand were retained in the system. A rectangular simulation box with margins of 10 Å around the protein was built using tleap, filled with TIP3P water molecules and charge-neutralized. AMBER 14 software (University of California, San Francisco) was used for the following steps: energy minimization (500 steps of steepest descent followed by 1000 steps of conjugate gradient minimization); gradual heating to 300 K in 1 ns, using harmonic restraints on non-hydrogen atoms; equilibration, with a gradual decrease on the restraints, applied on all non-hydrogen atoms of the system at a constant temperature of 300 K, using the Langevin thermostat and constant pressure of 1 atm using a Berendsen barostat. The coordinates were transferred to NAMD 2.11 (University of Illinois, Urbana-Champaign),[40] to perform a further stepwise heating step (10 K step, 20 ps) using a Langevin thermostat, followed by 30–40 ns of equilibration steps. The coordinates and velocities from the equilibrated system were extrapolated and used to start the actual MD simulations using τRAMD. A randomly oriented force (f) of magnitude 10 kcal mol^{-1} Å^{-1} was applied to the center of mass of the ligand. Every 100 fs, the orientation of the force was randomly redirected if the center of mass of the ligand had moved less than 0.025 Å. The τRAMD simulation was set to stop when the center of mass of the ligand had arrived at a maximum distance of 30 Å from its initial position. Sufficient sampling to compute the residence time was ensured by generating 50 independent simulations for each complex. The residence time (τ_{comp}) was defined as the time required for the ligand to dissociate from the protein in 50% of the trajectories. Statistical bootstrapping analysis was performed to determine τ_{comp}. The egress pathways of **5** from hPDE4D and TbrPDEB1 complexes were visually inspected with Visual Molecular Dynamics (VMD)[41] and depictions of the egress pathways were generated by tracking the coordinates of the center of mass of the ligand.

Interaction Fingerprint Analysis

Interaction fingerprints (apolar, face-to-face, and face-to-edge aromatic interactions, hydrogen bonds (acceptor or donor) and ionic interactions (cationic or anionic)) were calculated from the τRAMD and DUck trajectories of hPDE4D and TbrPDEB1 in complex with **5** and (4aR,8aS)-**7** using the OEChem Toolkit (OpenEye Scientific).[42] The program cpptraj was used process coordinate trajectories and data files, the "maskstr" selection string was applied to select all the atoms within 4 Å from any atom in residue $Gln^{Q.50}$, using a timeframe equal to 10. The frames were divided into 10 clusters based on the distance between $Gln^{Q.50}$ and the ligand. Water statistics were then calculated by retrieving the total number of HBs that involved water interactions of type ligand-water-$Gln^{Q.50}$. The number of HBs found in ligand-water-$Gln^{Q.50}$ interactions was normalized by the cluster size and reported in the heatmap.

Analysis of Water Sites in MD Trajectories

WATCLUST plugin tool,[25] implemented on VMD, was used to calculate the water sites (WS) around $Gln^{Q.50}$, using as input 2500 trajectory snapshots from the τRAMD simulation computed for hPDE4D and TbrPDEB1 in complex with **5** and (4aR,8aS)-**7** (PDB codes: 6HWO; 6GXQ), using default settings.

Water Network Generation and Scoring

WaterFLAP (version 2.2.1, Molecular Discovery) was used to place water molecules in the crystal structures of hPDE4D and TbrPDEB1 with **5** and (4aR,8aS)-**7** (PDB codes: 6HWO; 6GXQ). Initial placement of water molecules was performed using the Flapwater module at a radius of 10 Å from the ligand and recalculated iteratively with a GRID-based molecular interaction field (MIF) analysis, using as initial and final energy cutoff −8.0 kcal mol^{-1} and −1.0 kcal mol^{-1} respectively. The energetic properties of water molecules are then estimated and ranked as follows: favorable ($\Delta G < -1.0$ kcal mol^{-1}), bulk-like (ΔG between −1.0 and 2.0 kcal mol^{-1}), unfavorable (ΔG between 2.0 and 3.5 kcal mol^{-1}), and highly unfavorable ($\Delta G > 3.5$ kcal mol^{-1}).

Supporting Information Summary

The Supporting Information contains supplementary tables (Tables S1–S10), figures (Figures S1–S7) and analytical data. The authors have not cited additional references within the Supporting Information.

Acknowledgements

ChemMedChem

Research Article
doi.org/10.1002/cmdc.202400417

Chemistry
Europe
European Chemical
Societies Publishing

Conflict of Interests

The authors declare no competing financial interest.

Data Availability Statement

The data that support the findings of this study are available in the supplementary material of this article and through the corresponding author.

Keywords: Inhibitors · Selectivity · Kinetics · Structure-based drug discovery · Computer-aided drug design

[1] a) K. M. Orrling, C. Jansen, X. L. Vu, V. Balmer, P. Bregy, A. Shanmugham, P. England, D. Bailey, P. Cos, L. Maes, E. Adams, E. van den Bogaart, E. Chatelain, J. R. Ioset, A. van de Stolpe, S. Zorg, J. Veerman, T. Seebeck, G. J. Sterk, I. J. de Esch, R. Leurs, *J. Med. Chem.* **2012**, *55*, 8745–8756; b) C. Jansen, H. Wang, A. J. Kooistra, C. de Graaf, K. M. Orrling, H. Tenor, T. Seebeck, D. Bailey, I. J. de Esch, H. Ke, R. Leurs, *J. Med. Chem.* **2013**, *56*, 2087–2096; c) A. R. Blaazer, A. K. Singh, E. de Heuvel, E. Edink, K. M. Orrling, J. J. N. Veerman, T. van den Bergh, C. Jansen, E. Balasubramaniam, W. J. Mooij, H. Custers, M. Sijm, D. N. A. Tagoe, T. D. Kalejaiye, J. C. Munday, H. Tenor, A. Matheeussen, M. Wijtmans, M. Siderius, C. de Graaf, L. Maes, H. P. de Koning, D. S. Bailey, G. J. Sterk, I. J. P. de Esch, D. G. Brown, R. Leurs, *J. Med. Chem.* **2018**, *61*, 3870–3888; d) E. de Heuvel, A. K. Singh, E. Edink, T. van der Meer, M. van der Woude, P. Sadek, M. P. Krell-Jorgensen, T. van den Bergh, J. Veerman, G. Caljon, T. D. Kalejaiye, M. Wijtmans, L. Maes, H. P. de Koning, G. Jan Sterk, M. Siderius, I. J. P. de Esch, D. G. Brown, R. Leurs, *Bioorg. Med. Chem.* **2019**, *27*, 3998–4012.
[2] C. Jansen, A. J. Kooistra, G. K. Kanev, R. Leurs, I. J. de Esch, C. de Graaf, *J. Med. Chem.* **2016**, *59*, 7029–7065.
[3] P. D. Leeson, B. Springthorpe, *Nat. Rev. Drug Discov.* **2007**, *6*, 881–890.
[4] C. P. Page, D. Spina, in *Phosphodiesterases as Drug Targets. Handbook of Experimental Pharmacology* (Eds: S. Francis, M. Conti, M. Houslay), Vol. 204, Springer, Berlin, Heidelberg **2011**, 391–414.
[5] G. S. Baillie, G. S. Tejeda, M. P. Kelly, *Nat. Rev. Drug Discov.* **2019**, *18*, 770–796.
[6] a) J. Winquist, S. Geschwindner, Y. Xue, L. Gustavsson, D. Musil, J. Deinum, U. H. Danielson, *Biochemistry* **2013**, *52*, 613–626; b) A. Sandner, K. Ngo, J. Schiebel, A. I. M. Pizarroso, L. Schmidt, B. Wenzel, T. Steinmetzer, A. Ostermann, A. Heine, G. Klebe, *J. Med. Chem.* **2021**, *64*, 1611–1625.
[7] B. Srinivasan, *FEBS J.* **2023**, *290*, 2292–2305.
[8] V. Georgi, F. Schiele, B. T. Berger, A. Steffen, P. A. Marin Zapata, H. Briem, S. Menz, C. Preusse, J. D. Vasta, M. B. Robers, M. Brands, S. Knapp, A. Fernandez-Montalvan, *J. Am. Chem. Soc.* **2018**, *140*, 15774–15782.
[9] a) J. Michel, J. Tirado-Rives, W. L. Jorgensen, *J. Am. Chem. Soc.* **2009**, *131*, 15403–15411; b) A. Biela, N. N. Nasief, M. Betz, A. Heine, D. Hangauer, G. Klebe, *Angew. Chem. Int. Ed.* **2013**, *52*, 1822–1828; c) J. F. Darby, A. P. Hopkins, S. Shimizu, S. M. Roberts, J. A. Brannigan, J. P. Turkenburg, G. H. Thomas, R. E. Hubbard, M. Fischer, *J. Am. Chem. Soc.* **2019**, *141*, 15818–15826.
[10] A. C. Pan, D. W. Borhani, R. O. Dror, D. E. Shaw, *Drug Discov. Today* **2013**, *18*, 667–673.
[11] a) L. Liu, K. Michelsen, E. N. Kitova, P. D. Schnier, J. S. Klassen, *J Am Chem Soc* **2010**, *132*, 17658–17660; b) L. Deng, A. Broom, E. N. Kitova, M. R. Richards, R. B. Zheng, G. K. Shoemaker, E. M. Meiering, J. S. Klassen, *J. Am. Chem. Soc.* **2012**, *134*, 16586–16596
[12] P. Schmidtke, F. J. Luque, J. B. Murray, X. Barril, *J. Am. Chem. Soc.* **2011**, *133*, 18903–18910.
[13] A. Magarkar, G. Schnapp, A. K. Apel, D. Seeliger, C. S. Tautermann, *ACS Med. Chem. Lett.* **2019**, *10*, 324–328.
[14] T. Hufner-Wulsdorf, G. Klebe, *J. Chem. Inf. Model.* **2020**, *60*, 1818–1832.
[15] a) Q. Huai, H. Wang, Y. Sun, H. Y. Kim, Y. Liu, H. Ke, *Structure* **2003**, *11*, 865–873; b) K. Y. Zhang, G. L. Card, Y. Suzuki, D. R. Artis, D. Fong, S. Gillette, D. Hsieh, J. Neiman, B. L. West, C. Zhang, M. V. Milburn, S. H. Kim, J. Schlessinger, G. Bollag, *Mol. Cell* **2004**, *15*, 279–286; c) R. X. Xu, W. J. Rocque, M. H. Lambert, D. E. Vanderwall, M. A. Luther, R. T. Nolte, *J. Mol. Biol.* **2004**, *337*, 355–365; d) G. L. Card, B. P. England, Y. Suzuki, D. Fong, B. Powell, B. Lee, C. Luu, M. Tabrizizad, S. Gillette, P. N. Ibrahim, D. R. Artis, G. Bollag, M. V. Milburn, S. H. Kim, J. Schlessinger, K. Y. Zhang, *Structure* **2004**, *12*, 2233–2247.
[16] J. Veerman, T. van den Bergh, K. M. Orrling, C. Jansen, P. Cos, L. Maes, E. Chatelain, J. R. Ioset, E. E. Edink, H. Tenor, T. Seebeck, I. de Esch, R. Leurs, G. J. Sterk, *Bioorg. Med. Chem.* **2016**, *24*, 1573–1581.
[17] P. Cedervall, A. Aulabaugh, K. F. Geoghegan, T. J. McLellan, J. Pandit, *Proc. Natl. Acad. Sci. USA* **2015**, *112*, E1414–E1422.
[18] a) T. S. Olsson, M. A. Williams, W. R. Pitt, J. E. Ladbury, *J. Mol. Biol.* **2008**, *384*, 1002–1017; b) G. G. Ferenczy, G. M. Keserű, *Drug Discov. Today* **2010**, *15*, 919–932; c) B. Breiten, M. R. Lockett, W. Sherman, S. Fujita, M. Al-Sayah, H. Lange, C. M. Bowers, A. Heroux, G. Krilov, G. M. Whitesides, *J. Am. Chem. Soc.* **2013**, *135*, 15579–15584.
[19] E. Edink, P. Rucktooa, K. Retra, A. Akdemir, T. Nahar, O. Zuiderveld, R. van Elk, E. Janssen, P. van Nierop, J. van Muijlwijk-Koezen, A. B. Smit, T. K. Sixma, R. Leurs, I. J. de Esch, *J. Am. Chem. Soc.* **2011**, *133*, 5363–5371.
[20] M. Siderius, A. Shanmugham, P. England, T. van der Meer, J. P. Bebelman, A. R. Blaazer, I. J. de Esch, R. Leurs, *Anal. Biochem.* **2016**, *503*, 41–49.
[21] A. B. Burgin, O. T. Magnusson, J. Singh, P. Witte, B. L. Staker, J. M. Bjornsson, M. Thorsteinsdottir, S. Hrafnsdottir, T. Hagen, A. S. Kiselyov, L. J. Stewart, M. E. Gurney, *Nat. Biotechnol.* **2010**, *28*, 63–70.
[22] S. D. Rybalkin, T. R. Hinds, J. A. Beavo, *Methods Mol. Biol.* **2013**, *1020*, 51–62.
[23] S. Ruiz-Carmona, P. Schmidtke, F. J. Luque, L. Baker, N. Matassova, B. Davis, S. Roughley, J. Murray, R. Hubbard, X. Barril, *Nat. Chem.* **2017**, *9*, 201–206.
[24] D. B. Kokh, M. Amaral, J. Bomke, U. Gradler, D. Musil, H. P. Buchstaller, M. K. Dreyer, M. Frech, M. Lowinski, F. Vallee, M. Bianciotto, A. Rak, R. C. Wade, *J. Chem. Theory Comput.* **2018**, *14*, 3859–3869.
[25] E. D. Lopez, J. P. Arcon, D. F. Gauto, A. A. Petruk, C. P. Modenutti, V. G. Dumas, M. A. Marti, A. G. Turjanski, *Bioinformatics* **2015**, *31*, 3697–3699.
[26] M. Baroni, G. Cruciani, S. Sciabola, F. Perruccio, J. S. Mason, *J. Chem. Inf. Model.* **2007**, *47*, 279–294.
[27] E. de Heuvel, A. K. Singh, P. Boronat, A. J. Kooistra, T. van der Meer, P. Sadek, A. R. Blaazer, N. C. Shaner, D. S. Bindels, G. Caljon, L. Maes, G. J. Sterk, M. Siderius, M. Oberholzer, I. J. P. de Esch, D. G. Brown, R. Leurs, *Bioorg. Med. Chem.* **2019**, *27*, 4013–4029.
[28] a) T. Pantsar, P. D. Kaiser, M. Kudolo, M. Forster, U. Rothbauer, S. A. Laufer, *Nat. Commun.* **2022**, *13*, 569; b) N. Ansari, V. Rizzi, M. Parrinello, *Nat. Commun.* **2022**, *13*, 5438.
[29] S. Saubern, R. Guha, J. B. Baell, *Mol. Inform.* **2011**, *30*, 847–850.
[30] G. Winter, C. M. Lobley, S. M. Prince, *Acta Cryst. D Biol. Cryst.* **2013**, *69*, 1260–1273.
[31] C. Vonrhein, C. Flensburg, P. Keller, A. Sharff, O. Smart, W. Paciorek, T. Womack, G. Bricogne, *Acta Cryst. D Biol. Cryst.* **2011**, *67*, 293–302.
[32] W. Kabsch, *Acta Cryst. D Biol. Cryst.* **2010**, *66*, 133–144.
[33] P. R. Evans, G. N. Murshudov, *Acta Cryst. D Biol. Cryst.* **2013**, *69*, 1204–1214.
[34] M. D. Winn, C. C. Ballard, K. D. Cowtan, E. J. Dodson, P. Emsley, P. R. Evans, R. M. Keegan, E. B. Krissinel, A. G. Leslie, A. McCoy, S. J. McNicholas, G. N. Murshudov, N. S. Pannu, E. A. Potterton, H. R. Powell, R. J. Read, A. Vagin, K. S. Wilson, *Acta Cryst. D Biol. Cryst.* **2011**, *67*, 235–242.
[35] A. J. McCoy, R. W. Grosse-Kunstleve, P. D. Adams, M. D. Winn, L. C. Storoni, R. J. Read, *J. Appl. Cryst.* **2007**, *40*, 658–674.

[36] P. Emsley, B. Lohkamp, W. G. Scott, K. Cowtan, *Acta Cryst. D Biol. Cryst.* **2010**, *66*, 486–501.

[37] G. N. Murshudov, P. Skubak, A. A. Lebedev, N. S. Pannu, R. A. Steiner, R. A. Nicholls, M. D. Winn, F. Long, A. A. Vagin, *Acta Cryst. D Biol. Cryst.* **2011**, *67*, 355–367.

[38] C. J. Williams, J. J. Headd, N. W. Moriarty, M. G. Prisant, L. L. Videau, L. N. Deis, V. Verma, D. A. Keedy, B. J. Hintze, V. B. Chen, S. Jain, S. M. Lewis, W. B. Arendall, 3rd, J. Snoeyink, P. D. Adams, S. C. Lovell, J. S. Richardson, D. C. Richardson, *Protein Sci.* **2018**, *27*, 293–315.

[39] H. P. de Koning, M. K. Gould, G. J. Sterk, H. Tenor, S. Kunz, E. Luginbuehl, T. Seebeck, *J. Infect. Dis.* **2012**, *206*, 229–237.

[40] J. C. Phillips, D. J. Hardy, J. D. C. Maia, J. E. Stone, J. V. Ribeiro, R. C. Bernardi, R. Buch, G. Fiorin, J. Henin, W. Jiang, R. McGreevy, M. C. R. Melo, B. K. Radak, R. D. Skeel, A. Singharoy, Y. Wang, B. Roux, A. Aksimentiev, Z. Luthey-Schulten, L. V. Kale, K. Schulten, C. Chipot, E. Tajkhorshid, *J. Chem. Phys.* **2020**, *153*, 044130.

[41] W. Humphrey, A. Dalke, K. Schulten, *J. Mol. Graph.* **1996**, *14*, 33–38.

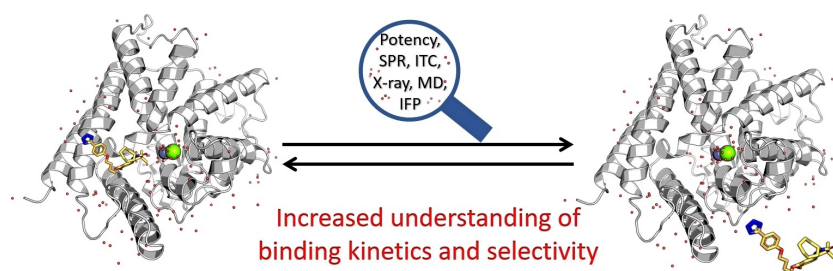[42] G. Marcou, D. Rognan, *J. Chem. Inf. Model.* **2007**, *47*, 195–207.

RESEARCH ARTICLE

Increased understanding of binding kinetics and selectivity

Phosphodiesterase (PDE) inhibitor selectivity and binding kinetics can be rationalized with the help of biophysical and computational methods. Water molecules have been found to influence the stability of a key hydrogen bond affecting the kinetic selectivity of inhibitors. Shielding this hydrogen bond from water is a design strategy that can provide more selective PDE inhibitors.

A. R. Blaazer, A. K. Singh, L. Zara, P. Boronat, L. J. Bautista, S. Irving, M. Majewski, X. Barril, M. Wijtmans, U. H. Danielson, G. J. Sterk, R. Leurs, J. E. van Muijlwijk-Koezen, D. G. Brown, I. J. P. de Esch*

The Role of Water Networks in Phosphodiesterase Inhibitor Dissociation and Kinetic Selectivity